ACS APPLIED MATERIALS & INTERFACES

Research Article

www.acsami.org

# Gold Embedded Maghemite Hybrid Nanowires and Their Gas Sensing Properties

Na-Mei Li, Kai-Min Li, Shun Wang, Ke-Qin Yang, Li-Jie Zhang, Qing Chen,* and Wei-Ming Zhang*

College of Chemistry & Materials Engineering, Wenzhou University, Wenzhou 325000, People's Republic of China

Supporting Information

**ABSTRACT:** Well-defined gold embedded maghemite hybrid nanowires are synthesized, and their structures are fully characterized. They are composed of porous $\gamma$-$Fe_2O_3$ shells and embedded gold nanoparticles (3−10 nm), which is novel and very different from the conventional "surface decoration" configuration. These hybrid nanowires are produced by the de-alloying of Au−Fe alloy nanowires and subsequent heat treatment. The reaction mechanism is proposed and validated. The results of X-ray diffraction, scanning electron microscopy, transmission electron microscopy, and thermogravimetry techniques prove consistently that the Fe composition of Au−Fe alloy nanowires change to $\gamma$-FeOOH first and then to $\gamma$-$Fe_2O_3$. The embedded gold particles are help to enhance the gas response properties of the hybrid nanowires, which is attributed to the nano open-circuit Schottky junctions between $\gamma$-$Fe_2O_3$ and the Au nanoparticles. The gas sensing experiment data with high repeatability demonstrate that these hybrid nanowires are excellent sensing materials, especially for ethanol, and have shown both high selectivity and high sensitivity.

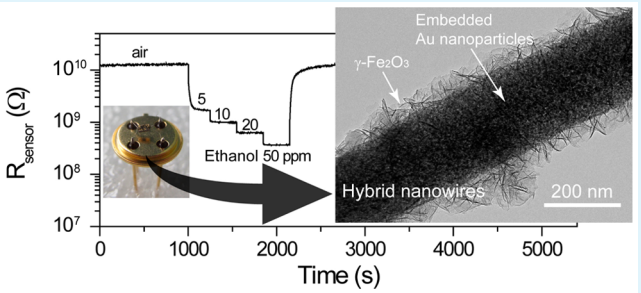


**KEYWORDS:** *hybrid nanowires, gold, maghemite, lepidocrocite, de-alloying, gas sensing*

## 1. INTRODUCTION

One-dimensional (1D) metal oxide semiconductors (MOSs) are regarded as ideal building blocks for chemical sensing applications.[1−3] MOSs such as $SnO_2$,[4] $In_2O_3$,[5−7] and iron oxides[8−10] have exhibited very good sensitivity in chemical gas sensors. The 1D MOS nanostructures are less agglomerated in thick gas sensing films and show improved performance when compared with their zero-dimensional (0D) analogues such as nanoparticles and nanocrystals.[1−3] It is also well-known that the response of gas sensing increases greatly as the crystal size decreases, especially smaller than the Debye length (typically several nm)[11] or the charge carrier depletion zone sizes.[4,12,13] In addition, nanopores in hollow or porous nanostructures can facilitate the gas transportation and ensure fast gas response kinetics.[14,15] Wang et al. reported porous $\alpha$−$Fe_2O_3$ nanowires by sintering organic iron precursor nanowires, which exhibited high gas sensitivity to flammable and corrosive gases.[9] It will be helpful to further enhance the 1D MOS gas sensing performance by creating nanoporosity and reducing the grain sizes in the structure.

Noble metal (NM) decoration of the MOSs has been proven as another efficient approach to boost the gas response performance, including sensitivity and selectivity.[4,10,16] A main challenge in the research of the gas sensor material is the preparation of multicompositional hierarchical/hollow structures which is functionalized by NM or other catalysts.[15] Such materials are ideal to obtain high sensitivity, high selectivity, as well as fast response and recovery kinetics. Currently most of such hybrid gas sensing materials are prepared by surface decoration. MOS base materials such as nanoparticles,[16−18] nanowires[4] or films[10] are fabricated first, and then NM particles are immobilized on the surfaces by vapor deposition,[4] RF sputtering,[10] or surface chemical reactions.[16−18] Hybrid nanostructures with the NM-on-MOS configurations show tremendous potentials in gas sensing applications, and their gas response characteristics are closely related to their unique structure.[4] It would be scientifically and practically important to synthesize hybrid gas materials with alternative configurations. NM-embedded-MOS hybrid configuration is another option,[19−25] and materials with such configuration exhibit very unique characteristics in photoanodic properties,[19,20] nanophotonics,[21−23] electrochromism,[24] and gas sensing.[25] NM-embedded-MOS nanofilms can be prepared by a two-step method: first NM nanoparticles are dispersed on a substrate, and then a MOS layer is covered on the top,[20,25,26] while, to the best of our knowledge, NM-embedded-MOS 1D nanowires can not be prepared with this strategy. Peapod-like Au nanoparticles embedded in MOS nanowires were normally synthesized by special designed vapor−liquid−solid (VLS) growth with liquid Au droplets as catalysts at high temperatures, including in $SiO_2$,[21] $Ga_2O_3$[22] and indium tin oxide[23] nanowires. Liu et al. reported the fabrication of peapod Pt@$CoAl_2O_4$ nanowires by the solid-state reaction of Co−Pt multilayer nanowires with the alumina wall of the anodic

Received: March 9, 2015
Accepted: May 1, 2015
Published: May 4, 2015





DOI: 10.1021/acsami.5b02087
ACS Appl. Mater. Interfaces 2015, 7, 10534−10540

Table 1. Electrodeposition Parameters, Compositions, and Brief Morphologies for All Samples Prepared in This Study

| | electrodeposition parameters | | | | | |
|---|---|---|---|---|---|---|
| sample index | $[Fe^{2+}]$ (mmol/L) | $[Au(CN)_2^-]$ (mmol/L) | current density ($mA/cm^2$) | compositions of assynthsized nanowires (Au atom-%) | compositions after de-alloying treatment (Au atom-%) | product morphologies |
| 1 | 500 | 0 | 10 | 0 | 0 | nanoflowers |
| 2 | 500 | 2.0 | 16 | 1.4 | 1.8 | transition state |
| 3 | 500 | 2.0 | 8.0 | 2.1 | 12 | inherited hybrid nanowires |
| 4 | 500 | 10 | 16 | 4.4 | 25 | inherited hybrid nanowires |
| 5 | 500 | 10 | 10 | 7.1 | 30 | inherited hybrid nanowires |
| 6 | 500 | 10 | 6.0 | 18 | 79 | inherited hybrid nanowires |
| 7 | 0 | 20 | 1.0 | 100 | | |

aluminum oxide (AAO) membranes in the heat.[27] All above 1D NM-embedded-MOS materials have the similar peapod structures, because the noble metal inclusions agglomerate into spherical "peas" to minimize their surface energies at high temperatures. Uniform NM dispersion in the MOS matrix is not energy favored in the above synthesis processes. Alternatively, solution chemistry based process must be involved to overcome this challenge. There are very few public reports on synthesis of 1D NM-embedded-MOS nanostructures in solution chemistry. Pyun and co-workers reported a method to produce $Co_3O_4$ nanowires with Au nanoparticles inclusions.[28] They prepared the nanowires via the colloid polymerization of the ferromagnetic Au−Co core−shell nanoparticles first, and followed by the oxidation of cobalt shells in the reorganized nanoparticles chains.

Herein, we report a new approach to produce Au embedded porous $\gamma$−$Fe_2O_3$ nanowires by a mild oxidation of Au−Fe alloy nanowires. Pulse electrodeposition is a mature technology to produce bimetallic barcode nanowires in a single bath, which has been well documented in literatures[27,29,30] and in our previous work.[31] Au−Fe barcode nanowires can be electrochemically fabricated using nanoporous templates in a mixed electroplating solution of high concentration of $FeSO_4$ and low concentration of $KAu(CN)_2$. Iron segments are electrochemically deposited at high current density, because the $KAu(CN)_2$ can only provide a very little portion of the cathodic current,[30,31] while, technically speaking, these iron segments are alloys of iron and gold. By carefully adjusting the current density and the composition of electroplating solution, the gold contents can be controlled in these alloys. Besides, a solution-based oxidation process is proposed to convert the iron to porous $\gamma$−$Fe_2O_3$ in the alloy nanowires, which is inspired by the industrial steel bluing process. The Au contents disperse evenly inside the resulting hybrid nanowires as isolated nanoparticles with a diameter of 3−10 nm, which are very different from the peapod-like structures. These hybrid NM-embedded-MOS nanowires may have great potential in nanophotonics and gas sensing applications.

## 2. MATERIALS AND METHODS

**2.1. Fabrication of Au−Fe Alloy Nanowires.** The Au−Fe alloy nanowires were electrochemically deposited into the pores of anodic aluminum oxide (AAO) membranes, in an electroplating bath containing $Fe^{2+}$ and $Au(CN)_2^-$ ions. The experimental apparatus was well documented in previous works.[30,31] Different parameters, listed in Table 1, were configured during the electrodeposition process to produce nanowires with different compositions. The AAO membranes were cleaned with deionized water and absolute alcohol several times and dried naturally after the electrodeposition. The resulted alloy nanowires were characterized by SEM (FEI Nova NanoSEM 200) directly in cross-section of the AAO membrane. Then the Ag backing layer was selectively removed by a mixture of ethanol, $H_2O_2$ and $NH_3{\cdot}H_2O$.[32] The X-ray diffraction (XRD, Bruker D8 Advance with Cu K$\alpha$ radiation) patterns of the alloy nanowires were recorded in the AAO membranes. For alloy composition analysis, part of the AAO membrane was completely digested in aqua regia. The resulting solution was diluted by deionized water (18.2 MΩ·cm) and analyzed by inductively coupled plasma optical emission spectrometry (ICP-OES, PerkinElmer Optima 8000) to determine the concentrations of Au and Fe.

**2.2. Synthesis of $\gamma$-FeOOH and $\gamma$-$Fe_2O_3$ Hybrid Nanowires.** A mixed solution (5 mL, containing NaOH 4.4 g and $NaNO_2$ 1.0 g) was heated to about 140 °C (slightly boiling) in oil bath.[33] A piece of AAO membrane with Au−Fe alloy nanowires (0.5 $cm^2$) was put into the hot solution, and it dissolved very quickly (about 2 min). The solution was heated for another 10 min, and it became yellowish (low Au content) or brown (high Au content) and nearly transparent in appearance. The solution was removed from the oil bath and poured into cool deionized water (100 mL). After settling for about 2 h, the precipitations were collected by centrifugation. The product was washed with deionized water several times, and then with absolute alcohol. Finally, it was dried in vacuum drying oven at 40 °C for about 10 h to get the $\gamma$-FeOOH hybrid nanowires. The $\gamma$-$Fe_2O_3$ hybrid nanowires were obtained by heating the $\gamma$-FeOOH hybrid nanowires at 350 °C in air or at 150 °C in vacuum (<1000 Pa) for 10 h.[34] The products were characterized by XRD, scanning electron microscopy (SEM), high-resolution transmission electron microscopy (HRTEM; FEI Tecnai G2 F30), and thermogravimetrics (TG, TA Instruments SDT Q600). All chemicals used in this work are of analytical reagent grade (Sinopharm Chemical Reagent Co. Ltd., China) and used as received.

**2.3. Gas Sensing Measurement.** The gas sensing properties of the gold−maghemite hybrid nanowires were evaluated by a homemade system. The hybrid nanowires were dispersed in alcohol and dropped on a micro planar-ceramic sensor chip (Hanwei Electronics Co., Ltd., China). Mass flow controllers (MFCs, D07-11C, Beijing Sevenstar Electronics Co., Ltd., China) were used to control the flow rates of all gases. A programmable dc power supply (Agilent E3640A) heated the sensor chips, and a source measurement unit (SMU, Keithley 2400) monitored the electric resistance of the sensing layer. The operating temperature was 210 °C in all tests.

## 3. RESULTS AND DISCUSSION

**3.1. Au−Fe Alloy Nanowires.** The Au−Fe alloy nanowires were prepared by electrodeposition in $Fe^{2+}$ and $Au(CN)_2^-$ mixed solution. The lower the cathodic current density and the higher concentration of $Au(CN)_2^-$, the higher the Au content in the resulted alloy nanowires.[30,31] Different electroplating bath compositions and current densities are configured and


DOI: 10.1021/acsami.5b02087
ACS Appl. Mater. Interfaces 2015, 7, 10534−10540

listed in Table 1, which are marked as samples 1−7. Sample 1 is pure Fe and sample 7 is pure Au for references. ICP-OES was employed to determine the compositions of the alloy nanowires, and the results are also listed in Table 1. The Au content increases from sample 2 (1.4 at-% Au) to sample 6 (18 at-% Au) as the current density decreases and the $Au(CN)_2^-$ concentration increases. Cross-sectional SEM characterizations of the resulted products confirm that well-defined nanowires are obtained in the AAO membranes after the electrodeposition in all samples, and a typical SEM image (sample 4, for example) is shown in Figure S1a (Supporting Information). The nanowires are about 200 nm in diameter (100−300 nm) and about 20 $\mu$m in length. Figure 1 shows the XRD patterns of all

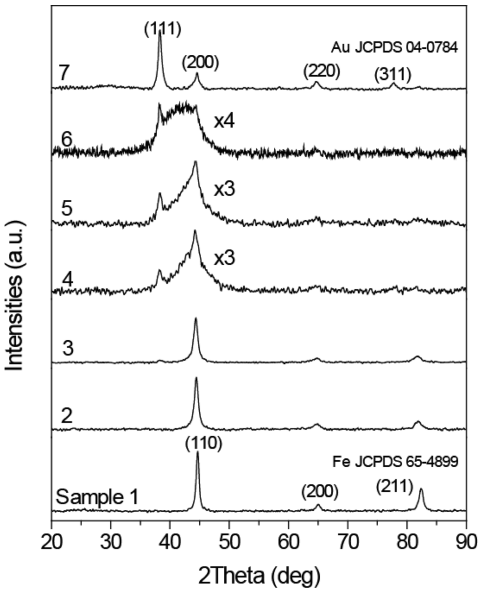


**Figure 1.** XRD patterns of the alloy nanowires. The samples are labeled from 1 to 7 as the Au contents increase (Table 1).

these samples. For samples 1 (pure Fe) and 7 (pure Au), all peaks are in good agreement with body-centered cubic (bcc) $\alpha$−Fe (JCPDS 65-4899) and face-centered cubic (fcc) Au (JCPDS 04-0784), respectively. For the pure Fe nanowires, the peak of the $\alpha$−Fe (110) crystal plane is sharp and high in intensity, and it shows good crystallinity, while as Au atoms are inserted into the nanowires, the crystallinity of Fe matrix begins to degrade. The XRD pattern of sample 2, which contains only 1.4 at-% of Au content, is very similar to that of the pure Fe (sample 1). However, the peak intensity of Fe (44.66°) becomes lower, and the peak is not as sharp as that of sample 1. As the Au content increases in the alloy nanowires from sample 3 to sample 7, the $\alpha$−Fe (110) peak (44.66°) decreases and Au (111) peak (38.18°) increases continuously. The XRD spectra here clearly show the transition process of bcc $\alpha$−Fe (sample 1) to fcc Au (sample 7). The broadening of the Fe diffraction peak (44.66°, in sample 4−6) indicates that the Au atoms exist as solid solution in the Fe matrix in these samples. The difference of atomic radius between Au and Fe atoms causes the lattice strain, which is the same as that in Au−Fe disordered alloy films prepared by face-to-face sputtering technique.[35] It is also reported that the bcc−fcc structural transformation occurs at about 80 at-% of Fe in AuFe alloy films,[35] which is exactly the same case in our work. The highest peak is $\alpha$−Fe (110) in samples with low Au contents (samples 1−5, 0−7.1 at-% Au), and it decreases in intensity and broadens in bandwidth as the Au content increases. The bcc Fe matrix remains in these samples, and the lattice strain successively increases as the Au content increases. When the Au content reaches about 20 at-% (sample 6, 18 at-% Au), a broad peak appears between Au (111) and $\alpha$−Fe (110) peaks (38.18−44.66°), indicating a transition state during the bcc−fcc structural transformation.

**3.2. De-alloying of the Au−Fe Nanowires.** As shown in Scheme 1, the removal of AAO membrane and the de-alloying

**Scheme 1. Brief Synthesis Process of the Hybrid Nanowires**

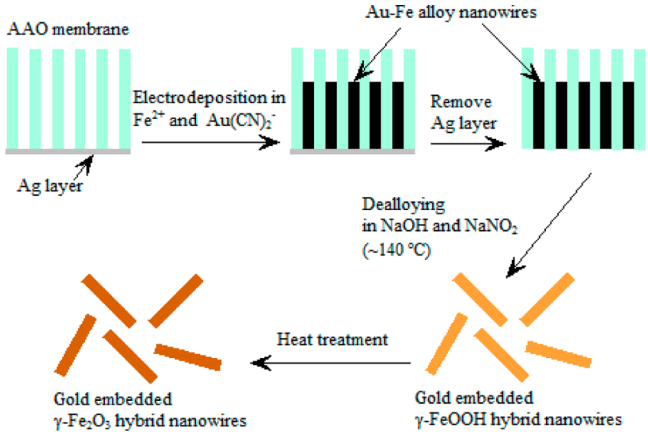


of Au−Fe nanowires occur at the same time in a hot mixture of NaOH and $NaNO_2$ solution. The similar recipe is usually used in steel bluing process, in which thin $Fe_3O_4$ protecting films are formed on the steel surfaces,[33] while both NaOH concentration and process temperature are higher in this work.

For Au−Fe alloy nanowires with Au content higher than 2 at-% (sample 3−6), inherited hybrid nanowires are obtained after the de-alloying process, and a typical morphology (sample 5, for example) is shown in Figure 2c. A large scale SEM image of another similar product (sample 4) is shown in Figure S1b (Supporting Information), and a high-resolution TEM image is also inserted. The hybrid nanowires have the same length as the Au−Fe nanowires, but the diameter is larger (~400 nm). As displayed in Figure 2a, for pure Fe nanowires (sample 1), the 1D structures change into nanoflowers with a diameter of ~200 nm. Between the two different transformation processes, the transition morphology appears in sample 2 (Figure 2b), and it has a similar nanoflowers structure with a tendency to form 1D nanowires. The morphologies of all samples after the de-alloying procedure are also listed in Table 1 briefly. ICP-OES analysis results indicate that the resulted hybrid nanowires are also consisted of Au and Fe, and no impurities such as Na and Al exist. The composition data from ICP results are also listed in Table 1. The Au contents are significantly higher in the hybrid nanowires than those in the Au−Fe alloy nanowires. Because Au is quite inert in the hot mixture of NaOH and $NaNO_2$, this composition change indicates a loss of Fe in the de-alloying process. For sample 3−6, the Au content is about 5 times higher in the hybrid nanowires than that in their Au−Fe alloy precursors, which manifests that ~80% of Fe are lost in this procedure.

The XRD pattern of the nanoflowers (Figure 3a) can be readily indexed as $\gamma$-FeOOH phase (lepidocrocite, JCPDS 76−2301). The diffraction peaks are pretty low and broad in shape, which indicates that the $\gamma$-FeOOH nanoflowers are not well


DOI: 10.1021/acsami.5b02087
ACS Appl. Mater. Interfaces 2015, 7, 10534−10540

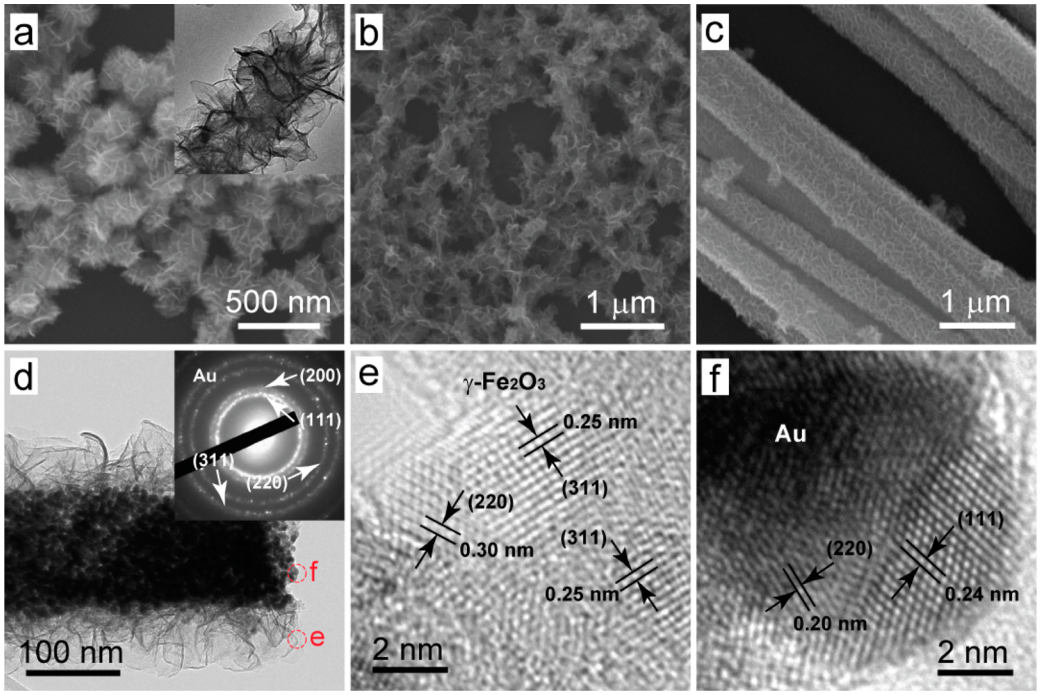


**Figure 2.** Typical SEM images of the as-synthesized de-alloying products, (a) sample 1, (b) sample 2, and (c) sample 5. (a, inset) Enlarged TEM image of the sample 1. (d) Low-magnification TEM image of an individual hybrid nanowire (sample 5) after being heated at 150 °C in vacuum and (inset) corresponding selected area electron diffraction pattern. HRTEM images of (e) selected area of $\gamma$–$Fe_2O_3$ shell and (f) an individual Au nanoparticle.

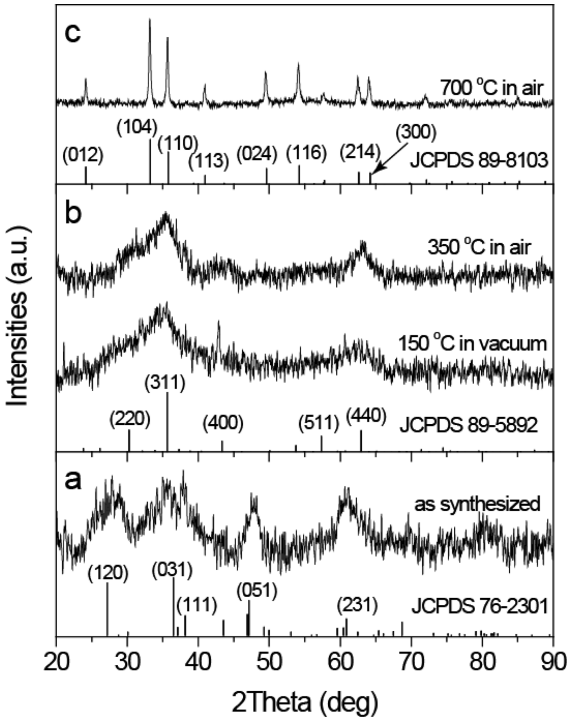


**Figure 3.** XRD patterns of the nanoflowers produced by de-alloying pure Fe nanowires. (a) As-synthesized nanoflowers, identified as $\gamma$-FeOOH (JCPDS 76-2301) with poor crystallinity. (b) After heat treatment at low temperatures, $\gamma$-$Fe_2O_3$ (JCPDS 89-5892) with poor crystalline is formed. (c) After heat treatment at high temperatures, $\alpha$-$Fe_2O_3$ (JCPDS 89-8103) with improved crystallinity is formed.

crystallized. The mean grain size is only 3–5 nm according to the Scherrer equation. In addition, the lepidocrocite–maghemite–hematite transition by heat treatment further confirms the structure (Figure 3b,c). The diffraction intensities of Au contents are much higher than $\gamma$-FeOOH, so only Au diffraction peaks appear in the XRD patterns of sample 3–6, and the patterns are similar to that of sample 7 in Figure 1. TEM characterization reveals that the hybrid nanowires have $\gamma$-FeOOH shells. The wrinkled thin nanosheets in these shells (Figure S1b, inset, Supporting Information) and in the nanoflowers (Figure 2a, inset) are identical in appearances.

In the conventional steel bluing process, thin $Fe_3O_4$ protecting films are formed on the steel surfaces in two steps. First, part of the iron atoms are oxidized and dissolved according to the following equations:

$$3Fe + 5NaOH + NaNO_2 \rightarrow 3Na_2FeO_2 + H_2O + NH_3\uparrow \quad (1)$$

$$6Na_2FeO_2 + NaNO_2 + 5H_2O \rightarrow 6NaFeO_2 + 7NaOH + NH_3\uparrow \quad (2)$$

Then, $Na_2FeO_2$ and $NaFeO_2$ react to form $Fe_3O_4$, which has lower solubility in the system:

$$Na_2FeO_2 + 2NaFeO_2 + 2H_2O \rightarrow Fe_3O_4 \downarrow + 4NaOH \quad (3)$$

After the formation of continuous $Fe_3O_4$ films, the bulk Fe will separate from the solution, and the reaction terminates. In the current work, both NaOH concentration and process temperature are higher, there will be no precipitate and all Fe will dissolve in the solution as $NaFeO_2$:

$$2Fe + NaOH + NaNO_2 + H_2O \rightarrow 2NaFeO_2 + NH_3\uparrow \quad (4)$$

As the solution is cooled and diluted, $\gamma$–FeOOH will precipitate:


DOI: 10.1021/acsami.5b02087
ACS Appl. Mater. Interfaces 2015, 7, 10534–10540

$$NaFeO_2 + H_2O \rightarrow NaOH + FeOOH\downarrow \quad (5)$$

For pure Fe sample, it dissolves completely as $NaFeO_2$ first. When it precipitates as $\gamma$−FeOOH, homogeneous nucleation is involved and uniform flower-like nanoparticles (~200 nm) are formed. While for Au−Fe alloy samples, porous Au nanowires remain in the solution as heterogeneous nuclei, and $\gamma$−FeOOH grow on the surface of Au nanoparticles. To validate this reaction mechanism, we replaced Fe nanowires with $Fe_2(SO_4)_3$ salt in the de-alloying process, and $\gamma$−FeOOH product with identical structure and morphology was obtained.

**3.3. Topotactic Phase Transition from $\gamma$-FeOOH to $\gamma$-$Fe_2O_3$.** It is well-known that $\gamma$-FeOOH transforms into $\gamma$-$Fe_2O_3$ first and then $\alpha$-$Fe_2O_3$ by dry heating.[34,36] The former transformation temperature is between 200 and 280 °C in air, and it drops to 120 °C under vacuum.[34] With the help of TG analysis, the phase transition of $\gamma$-FeOOH nanoflowers (Figure 2a) is better understood, and the result is shown in Figure S2 (Supporting Information). The weight loss is 13.5 wt %, which is in accord with the theoretical value (10.1 wt %, from $\gamma$-FeOOH to $\gamma$-$Fe_2O_3$). Figure 3 shows the XRD patterns of the nanoflowers before and after various heat treatments. For the moderately heated samples (350 °C in air or 150 °C in vacuum), XRD patterns (Figure 3b) agree with $\gamma$-$Fe_2O_3$ (maghemite, JCPDS 89-5892). This transition from $\gamma$-FeOOH to $\gamma$-$Fe_2O_3$ is topotactic, in which the oxygen framework remains intact while the hydroxyl groups are removed and the Fe atoms are redistributed.[36] So it is possible to keep the nanoflowers morphologies during this phase transition. The mean grain size remains unchanged (3−5 nm) in this process according to the Scherrer equation. Figure S3 (Supporting Information) shows the SEM images of the nanoflowers before and after the heat treatment, it is confirmed that the sample morphologies keep unchanged after heated at both 150 °C in vacuum (Figure S3b, Supporting Information) and 350 °C in air (Figure S3c, Supporting Information). The sample convert to $\alpha$-$Fe_2O_3$ (hematite, JCPDS 89-8103) after heated at 700 °C in air, and the corresponding XRD pattern is shown in Figure 3c. The nanosheets consisting of the nanoflowers disappear and transform into nanoparticles (Figure S3d, Supporting Information). Maghemite has inverse spinel structure, while hematite is isostructural with corundum. Formation and growth of hematite nuclei are involved during the transition, and the flower morphology collapses. The mean grain size increases to about 50 nm according to the Scherrer equation from Figure 3c.

To retain the structure of hybrid nanowires completely, we selected heat treatment at low temperature (150 °C) in vacuum for all samples used in gas sensing tests. Figure 2d−f provide detailed structure investigations of the resulted $\gamma$-$Fe_2O_3$ hybrid nanowires by TEM and electron diffraction. Figure 2d is a typical low magnification TEM image of the heat-treated hybrid nanowire. Gold nanoparticles (<10 nm) are embedded in a porous $\gamma$-$Fe_2O_3$ nanowire. The outer shell of the $\gamma$-$Fe_2O_3$ exhibits an identical appearance with $\gamma$-FeOOH precursor shown in the inset of Figure 2a. The inset in Figure 2d shows the corresponding selected area electron diffraction (SAED) pattern, which is identified as diffraction rings of polycrystalline metal Au. No signals from the $\gamma$-$Fe_2O_3$ are observed, which is similar to that in XRD characterization. Figure 2e shows the atomic resolution lattices image of the $\gamma$-$Fe_2O_3$ shell in the hybrid nanowires, in which the spacing of lattice related to (311) and (200) crystal planes is illustrated. The crystal domains are very small (<5 nm) in the image, which indicates that the $\gamma$-$Fe_2O_3$ shell is poorly crystallized and explains why no signals from Fe species are observed in both XRD and SAED patterns. Most gold nanoparticles swaddled by the $\gamma$-$Fe_2O_3$ shell have a diameter of 5−10 nm, Figure 2f is the HRTEM image of an individual gold nanoparticle in a hybrid nanowire. There are two different domains with lattice spacing of 0.2 and 0.24 nm, which correspond to (220) and (111) Au crystal planes, respectively.

**3.4. Gas Sensing Properties of the $\gamma$-$Fe_2O_3$ Hybrid Nanowires.** Iron oxides alone are good gas sensing materials,[8,9,37,38] and their sensing performances can be further enhanced by introducing noble metal additives, especially gold.[10,16,17] Currently the Au nanoparticles are decorated on the surface of iron oxides in most of these public literatures, and it is intriguing to figure out what will happen to the gas sensing performance if gold nanoparticles are embedded in the iron oxide matrix. Gas responses to $H_2$ and ethanol at different temperatures (76 to 302 °C) are shown in Figure S4 (Supporting Information), and all samples are heat treated at 150 °C in vacuum before the gas sensing tests. It is clearly indicated that at 210 °C all samples exhibit the best sensor sensitivity. Figure S5a (Supporting Information) shows the sensitivity responses of sensors based on different $\gamma$-$Fe_2O_3$ hybrid nanowires in 250 ppm of $H_2$. It is distinct that the sensitivity increases as the Au content increases to about 30 at-%. In sample 6 the Au content is very high (79 at-%), and the gold nanoparticles in the nanowires may contact with each other. The outer MOS shells are electrically short-circuited by these Au nanoparticles, so this sample shows no gas sensitivity at all. The sensor resistance of sample 6 is as low as 21.9 Ω at room temperature, and it increases to 26.3 Ω at sensor operation temperature (210 °C). The relationship between the resistance and temperature is similar to that of the pure metallic gold. While all remaining sensors based on other samples (sample 1−5) have much higher resistance (as high as $10^{10}$ Ω). Because the gold nanoparticles are embedded in the hybrid nanowires, the enhancement of gas sensing cannot be ascribed to the "chemical mechanism" involving catalytic dissociation of molecular oxygen and spillover effect.[4] Because the molecular oxygen may have a little chance to contact the Au nanoparticles in our hybrid nanowires, the "electronic mechanism" may explain the enhancement well.[4] As an *n*-type semiconductor (the sensor resistance decreases in reducing gases), the electrons in $\gamma$-$Fe_2O_3$ will flow to the Au nanoparticles to form open-circuit Schottky junctions.[12,39]

Besides $H_2$, the sensing properties to other reducing gases, such as ethanol, carbon monoxide and methane, are also worthy to evaluate. Because the sensor based on sample 5 has demonstrated the highest sensitivity to $H_2$, it is chosen naturally for the following investigation. The corresponding responses are shown in Figure S5b (Supporting Information). The sensitivity to ethanol is much higher than other gases even though the concentration of ethanol is much lower. These results show that the $\gamma$-$Fe_2O_3$ hybrid nanowires are very suitable materials for ethanol sensors because of the higher sensitivity and selectivity. More details about the real-time gas sensing curves of the hybrid nanowires (sample 5) can be found in Figure 4. In all test cycles (Figure 4a) the responses and recoveries are nearly the same, which means perfect sensitivity and stability. The response and recovery time (define as time to reach 90% of the equilibrium value) are also calculated in the inset, which are 7 and 65 s, respectively. Not only the switching


DOI: 10.1021/acsami.5b02087
ACS Appl. Mater. Interfaces 2015, 7, 10534−10540

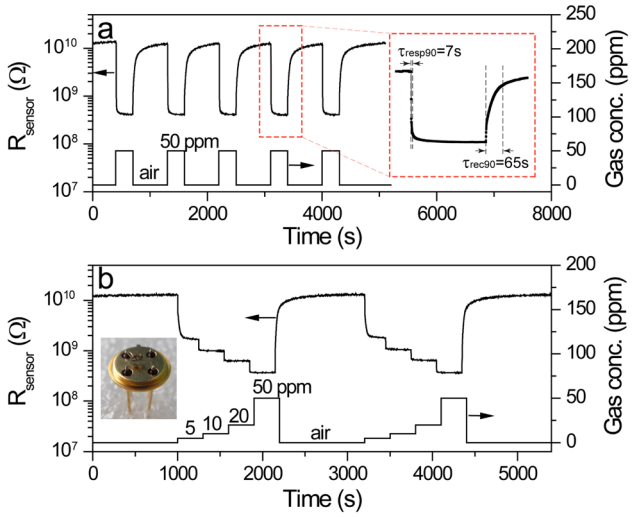


**Figure 4.** Gas sensing properties of the Au embedded $\gamma$-$Fe_2O_3$ hybrid nanowires (sample 5). (a) On–off responses in 50 ppm ethanol. The responding and recovering time shown in the red square. (b) Step responses to ethanol gases with concentrations from 5 to 50 ppm and (inset) photograph of the sensor device used.

response, the stair response in ethanol gases with different concentrations has also been studied carefully and demonstrated in Figure 4b. Four concentrations in multiplication (5, 10, 20, 50 ppm) in synthetic air are chosen. It remains excellent sensing performance in multiple cycles. The logarithm linearity relationship between sensor resistance and ethanol concentrations is calculated and shown in Figure S6 (Supporting Information). The good linearity is favored for practical sensing applications. The gas responses in Figure 4 suggest a sensing mechanism of surface chemisorptions of ethanol molecules. $\gamma$–$Fe_2O_3$ shells of the hybrid nanowires are n-type semiconductors, and free electrons are charge carriers. On one hand, the electrons in conduction band of $\gamma$-$Fe_2O_3$ will flow to the Au nanoparticles to form open-circuit Schottky junctions, as mentioned previously.[12,39] On the other hand, oxygen and moisture are absorbed on the semiconductor surfaces in ambient air, which also extracted electrons from the conduction band of semiconductor to form absorbed $O_2^-$ and $OH^-$ groups. Significant depletion layers are formed on the $\gamma$-$Fe_2O_3$ surfaces, so the hybrid nanowires exhibit very high resistance (>$10^{10}$ Ω) in air even at the operating temperature (210 °C). After the sensor was exposed to ethanol vapor, gas molecules are chemically absorbed on the semiconductor surface and oxidized into acetaldehyde and then carbon dioxide by the absorbed $O_2^-$ and $OH^-$.[9] In this oxidation process, some of the trapped electrons will be released and transfer back to the semiconductor, causing a dramatic decrease of sensor resistance.

It is validated that Au nanoparticles as additives are quite effective to enhance the gas sensitivities of iron oxide materials, no matter where the Au nanoparticles are located. The sensor sensitivity of gold-maghemite hybrid nanowires (35.1 for 50 ppm ethanol) is even higher than $\alpha$–$Fe_2O_3$ decorated by Au nanoparticles[16] (14 for 100 ppm ethanol) and Au-functionalized hematite nanospindles[17] (6 for 50 ppm ethanol). In addition, the sensor-array based electronic noses (eNose) rely heavily on the differences of the sensor characteristics.[40] The NM-embedded-MOS hybrid nanowires in this study may provide extra options to increase the variety of sensor arrays in eNose system and, thereby, to increase the dimension of data output.[40]

## 4. CONCLUSIONS

Well-defined gold embedded $\gamma$-FeOOH hybrid nanowires are prepared by direct de-alloying of Au–Fe alloy nanowires, which are electrochemically deposited in mixed solutions of $Fe^{2+}$ and $Au(CN)_2^-$. The reaction mechanism is proposed and validated, and the Au contents in the resulted hybrid nanowires can be adjusted easily by changing parameters during the electrodeposition process. After heated at 150 °C in vacuum, the $\gamma$-FeOOH hybrid nanowires will convert to $\gamma$-$Fe_2O_3$ hybrid nanowires and retain the microcosmic structures perfectly. The final hybrid nanowires have outer shells consisting of wrinkled $\gamma$-$Fe_2O_3$ nanosheets, and Au nanoparticles are embedded. These hybrid nanowires show good sensing performances and are promising for use in ethanol sensors with high sensitivity and high selectivity.

## ■ ASSOCIATED CONTENT

### Ⓢ Supporting Information

Supplementary images of SEM, TEM, TG and gas sensing characterizations. The Supporting Information is available free of charge on the ACS Publications website at DOI: 10.1021/acsami.5b02087.

## ■ AUTHOR INFORMATION

### Corresponding Authors

*Fax/Tel: +86-577-86689300. E-mail: chenqing@iccas.ac.cn.
*Fax/Tel: +86-577-86689300. E-mail: weiming@iccas.ac.cn.

### Notes

The authors declare no competing financial interest.

## ■ ACKNOWLEDGMENTS

The authors are grateful for financial support from the National Natural Science Foundation of China (Project Nos. 21203139, 21003097, and 61471270).

## ■ REFERENCES

(1) Kolmakov, A.; Moskovits, M. Chemical Sensing and Catalysis by One-Dimensional Metal-Oxide Nanostructures. *Annu. Rev. Mater. Res.* **2004**, *34* (1), 151–180.
(2) Chen, P.-C.; Shen, G.; Zhou, C. Chemical Sensors and Electronic Noses Based on 1-D Metal Oxide Nanostructures. *IEEE Trans. Nanotechnol.* **2008**, *7* (6), 668–682.
(3) Comini, E.; Baratto, C.; Faglia, G.; Ferroni, M.; Vomiero, A.; Sberveglieri, G. Quasi-One-Dimensional Metal Oxide Semiconductors: Preparation, Characterization and Application As Chemical Sensors. *Prog. Mater. Sci.* **2009**, *54* (1), 1–67.
(4) Kolmakov, A.; Klenov, D. O.; Lilach, Y.; Stemmer, S.; Moskovits, M. Enhanced Gas Sensing by Individual $SnO_2$ Nanowires and Nanobelts Functionalized with Pd Catalyst Particles. *Nano Lett.* **2005**, *5* (4), 667–673.
(5) Li, C.; Zhang, D.; Liu, X.; Han, S.; Tang, T.; Han, J.; Zhou, C. $In_2O_3$ Nanowires as Chemical Sensors. *Appl. Phys. Lett.* **2003**, *82* (10), 1613–1615.
(6) Zhang, D.; Liu, Z.; Li, C.; Tang, T.; Liu, X.; Han, S.; Lei, B.; Zhou, C. Detection of $NO_2$ down to ppb Levels Using Individual and Multiple $In_2O_3$ Nanowire Devices. *Nano Lett.* **2004**, *4* (10), 1919–1924.
(7) Zhongming, Z.; Kai, W.; Zengxing, Z.; Jiajun, C.; Weilie, Z. The Detection of $H_2S$ at Room Temperature by Using Individual Indium Oxide Nanowire Transistors. *Nanotechnology* **2009**, *20* (4), 045503.


DOI: 10.1021/acsami.5b02087
*ACS Appl. Mater. Interfaces* 2015, 7, 10534–10540

(8) Chen, J.; Xu, L.; Li, W.; Gou, X. $\alpha$-$Fe_2O_3$ Nanotubes in Gas Sensor and Lithium-Ion Battery Applications. *Adv. Mater.* **2005**, *17* (5), 582−586.
(9) Wang, G.; Gou, X.; Horvat, J.; Park, J. Facile Synthesis and Characterization of Iron Oxide Semiconductor Nanowires for Gas Sensing Application. *J. Phys. Chem. C* **2008**, *112* (39), 15220−15225.
(10) Peeters, D.; Barreca, D.; Carraro, G.; Comini, E.; Gasparotto, A.; Maccato, C.; Sada, C.; Sberveglieri, G. Au/$\varepsilon$-$Fe_2O_3$ Nanocomposites as Selective $NO_2$ Gas Sensors. *J. Phys. Chem. C* **2014**, *118* (22), 11813−11819.
(11) Xu, C.; Tamaki, J.; Miura, N.; Yamazoe, N. Grain Size Effects on Gas Sensitivity of Porous $SnO_2$-based Elements. *Sens. Actuators, B* **1991**, *3* (2), 147−155.
(12) Zhdanov, V. P. nm-Sized Metal Particles on a Semiconductor Surface, Schottky Model, etc. *Surf. Sci.* **2002**, *512* (1−2), L331−L334.
(13) Chen, C.-Y.; Retamal, J. R. D.; Wu, I. W.; Lien, D.-H.; Chen, M.-W.; Ding, Y.; Chueh, Y.-L.; Wu, C.-I.; He, J.-H. Probing Surface Band Bending of Surface-Engineered Metal Oxide Nanowires. *ACS Nano* **2012**, *6* (11), 9366−9372.
(14) Hoa, N. D.; Van Quy, N.; Jung, H.; Kim, D.; Kim, H.; Hong, S.-K. Synthesis of Porous CuO Nanowires and Its Application to Hydrogen Detection. *Sens. Actuators, B* **2010**, *146* (1), 266−272.
(15) Lee, J.-H. Gas Sensors Using Hierarchical and Hollow Oxide Nanostructures: Overview. *Sens. Actuators, B* **2009**, *140* (1), 319−336.
(16) Xianghong, L.; Jun, Z.; Xianzhi, G.; Shihua, W.; Shurong, W. Porous $\alpha$-$Fe_2O_3$ Decorated by Au Nanoparticles and Their Enhanced Sensor Performance. *Nanotechnology* **2010**, *21* (9), 095501.
(17) Zhang, J.; Liu, X.; Wang, L.; Yang, T.; Guo, X.; Wu, S.; Wang, S.; Zhang, S. Au-Functionalized Hematite Hybrid Nanospindles: General Synthesis, Gas Sensing, and Catalytic Properties. *J. Phys. Chem. C* **2011**, *115* (13), 5352−5357.
(18) Bao, J.; Chen, W.; Liu, T.; Zhu, Y.; Jin, P.; Wang, L.; Liu, J.; Wei, Y.; Li, Y. Bifunctional Au-$Fe_3O_4$ Nanoparticles for Protein Separation. *ACS Nano* **2007**, *1* (4), 293−298.
(19) Hida, Y.; Kozuka, H. Photoanodic Properties of Sol−Gel-derived Iron Oxide Thin Films with Embedded Gold Nanoparticles: Effects of Polyvinylpyrrolidone in Coating Solutions. *Thin Solid Films* **2005**, *476* (2), 264−271.
(20) Thimsen, E.; Le Formal, F.; Grätzel, M.; Warren, S. C. Influence of Plasmonic Au Nanoparticles on the Photoactivity of $Fe_2O_3$ Electrodes for Water Splitting. *Nano Lett.* **2011**, *11* (1), 35−43.
(21) Hu, M.-S.; Chen, H.-L.; Shen, C.-H.; Hong, L.-S.; Huang, B.-R.; Chen, K.-H.; Chen, L.-C. Photosensitive Gold-nanoparticle-embedded Dielectric Nanowires. *Nat. Mater.* **2006**, *5* (2), 102−106.
(22) Hsieh, C.-H.; Chou, L.-J.; Lin, G.-R.; Bando, Y.; Golberg, D. Nanophotonic Switch: Gold-in-$Ga_2O_3$ Peapod Nanowires. *Nano Lett.* **2008**, *8* (10), 3081−3085.
(23) Kim, H.; Park, S.; Jin, C.; Lee, C. Enhanced Photoluminescence in Au-Embedded ITO Nanowires. *ACS Appl. Mater. Interfaces* **2011**, *3* (12), 4677−4681.
(24) Nam, Y. S.; Park, H.; Magyar, A. P.; Yun, D. S.; Pollom, T. S.; Belcher, A. M. Virus-Templated Iridium Oxide-Gold Hybrid Nanowires for Electrochromic Application. *Nanoscale* **2012**, *4* (11), 3405−3409.
(25) Buso, D.; Post, M.; Cantalini, C.; Mulvaney, P.; Martucci, A. Gold Nanoparticle-Doped $TiO_2$ Semiconductor Thin Films: Gas Sensing Properties. *Adv. Funct. Mater.* **2008**, *18* (23), 3843−3849.
(26) Byoungjun, P.; Kyoungah, C.; Hyunsuk, K.; Sangsig, K. Capacitance Characteristics of MOS Capacitors Embedded with Colloidally Synthesized Gold Nanoparticles. *Semicond. Sci. Technol.* **2006**, *21* (7), 975.
(27) Liu, L.; Lee, W.; Scholz, R.; Pippel, E.; Gösele, U. Tailor-Made Inorganic Nanopeapods: Structural Design of Linear Noble Metal Nanoparticle Chains. *Angew. Chem., Int. Ed.* **2008**, *47* (37), 7004−7008.
(28) Kim, B. Y.; Shim, I.-B.; Araci, Z. O.; Saavedra, S. S.; Monti, O. L. A.; Armstrong, N. R.; Sahoo, R.; Srivastava, D. N.; Pyun, J. Synthesis and Colloidal Polymerization of Ferromagnetic Au−Co Nanoparticles into Au−$Co_3O_4$ Nanowires. *J. Am. Chem. Soc.* **2010**, *132* (10), 3234−3235.
(29) Choi, J.-r.; Oh, S. J.; Ju, H.; Cheon, J. Massive Fabrication of Free-Standing One-Dimensional Co/Pt Nanostructures and Modulation of Ferromagnetism via a Programmable Barcode Layer Effect. *Nano Lett.* **2005**, *5* (11), 2179−2183.
(30) Lee, J. H.; Wu, J. H.; Liu, H. L.; Cho, J. U.; Cho, M. K.; An, B. H.; Min, J. H.; Noh, S. J.; Kim, Y. K. Iron−Gold Barcode Nanowires. *Angew. Chem., Int. Ed.* **2007**, *46* (20), 3663−3667.
(31) Zhang, W.-M.; Hu, J.-S.; Ding, H.-T.; Wan, L.-J.; Song, W.-G. Programmed Fabrication of Bimetallic Nanobarcodes for Miniature Multiplexing Bioanalysis. *Anal. Chem.* **2009**, *81* (7), 2815−2818.
(32) Banholzer, M. J.; Osberg, K. D.; Li, S.; Mangelson, B. F.; Schatz, G. C.; Mirkin, C. A. Silver-Based Nanodisk Codes. *ACS Nano* **2010**, *4* (9), 5446−5452.
(33) Zhang, Y.; Hu, R.; Xiang, R. *Handbook of Electroplating (in Chinese)*. 3rd ed.; National Defense Industry Press: Beijing, 2007.
(34) Cornell, R. M.; Schwertmann, U. *The Iron Oxides: Structure, Properties, Reactions, Occurences and Uses*. Wiley-VCH: Weinheim, 2003.
(35) Hyun, Y. H.; Lee, Y. P.; Kudryavtsev, Y. V.; Gontarz, R. Properties of Au−Fe Disordered Alloy Films near the fcc−bcc Structural Transformation. *J. Korean. Phys. Soc.* **2003**, *43* (4), 625−628.
(36) Gendler, T. S.; Shcherbakov, V. P.; Dekkers, M. J.; Gapeev, A. K.; Gribov, S. K.; McClelland, E. The Lepidocrocite−Maghemite−Haematite Reaction Chain—I. Acquisition of Chemical Remanent Magnetization by Maghemite, Its Magnetic Properties and Thermal Stability. *Geophys. J. Int.* **2004**, *160* (3), 815−832.
(37) Dou, Z.-F.; Cao, C.-Y.; Wang, Q.; Qu, J.; Yu, Y.; Song, W.-G. Synthesis, Self-Assembly, and High Performance in Gas Sensing of X-Shaped Iron Oxide Crystals. *ACS Appl. Mater. Interfaces* **2012**, *4* (10), 5698−5703.
(38) Capone, S.; Manera, M. G.; Taurino, A.; Siciliano, P.; Rella, R.; Luby, S.; Benkovicova, M.; Siffalovic, P.; Majkova, E. $Fe_3O_4$/$\gamma$-$Fe_2O_3$ Nanoparticle Multilayers Deposited by the Langmuir−Blodgett Technique for Gas Sensors Application. *Langmuir* **2014**, *30* (4), 1190−1197.
(39) Korobchevskaya, K.; George, C.; Manna, L.; Comin, A. Effect of Morphology on Ultrafast Carrier Dynamics in Asymmetric Gold−Iron Oxide Plasmonic Heterodimers. *J. Phys. Chem. C* **2012**, *116* (51), 26924−26928.
(40) Röck, F.; Barsan, N.; Weimar, U. Electronic Nose: Current Status and Future Trends. *Chem. Rev.* **2008**, *108* (2), 705−725.


DOI: 10.1021/acsami.5b02087
*ACS Appl. Mater. Interfaces* 2015, 7, 10534−10540